Materials & Design 222 (2022) 111060

Contents lists available at ScienceDirect

Materials & Design

journal homepage: www.elsevier.com/locate/matdes

M-site solid solution of vanadium enables the promising mechanical and high-temperature tribological properties of Cr_2AlC coating

Zhenyu Wang [a], Cuicui Wang [a,b], Yupeng Zhang [a], Aiying Wang [a,b], Peiling Ke [a,b,c,*]

[a] Key Laboratory of Marine Materials and Related Technologies, Zhejiang Key Laboratory of Marine Materials and Protective Technologies, Ningbo Institute of Materials Technology and Engineering, Chinese Academy of Sciences, Ningbo 315201, China
[b] Center of Materials Science and Optoelectronics Engineering, University of Chinese Academy of Sciences, Beijing 100049, China
[c] Ningbo New Material Testing and Evaluation Center Co. Ltd, Ningbo 315048, China

HIGHLIGHTS

- Cr_2AlC and $(Cr,V)_2AlC$ coatings with a small amount of Cr were prepared by hybrid arc/magnetron sputtering followed by post-annealing.
- The hardness and toughness of the Cr_2AlC coating was enhanced simultaneously when Cr was partially substituted with V.
- Cr_2AlC had a relatively low COF and wear rate at 900 °C due to the existence of Cr_2O_3 oxides.
- $(Cr_{0.53}V_{0.47})_2AlC$ obtained excellent tribological properties due to the formation of molten V_2O_5 wrapped (Cr, Al)$_2O_3$ hard crystal grains.

GRAPHICAL ABSTRACT

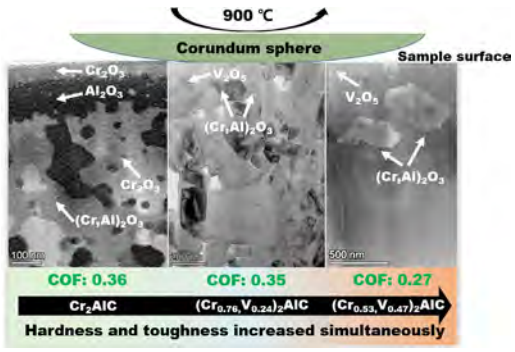

ARTICLE INFO

Article history:
Received 19 May 2022
Revised 3 August 2022
Accepted 12 August 2022
Available online 17 August 2022

Keywords:
Cr_2AlC
M-site solid solution
Hard-yet-tough
High-temperature friction

ABSTRACT

Cr_2AlC MAX phase coating exhibited excellent oxidation resistance and hot corrosion, but it typically suffered from low hardness and toughness as well as lack of lubrication at high temperature. With a solid solution design on M-site, we demonstrated that the hardness of the Cr_2AlC MAX phase coating was enhanced by 34.3% when Cr was partially substituted with V (47 at.%), and the coating toughness was improved simultaneously. Furthermore, according to the high-temperature tribometer test, both the friction coefficient and the wear rate of the coatings at 900 °C against Al_2O_3 balls were significantly reduced at 47 at.% V. This could be attributed to the formation of a large number of molten V_2O_5 wrapped (Cr, Al)$_2O_3$ hard crystal grains, which not only provided a wide range of liquid-phase lubrication, but also prevented the coating from being apt to wear out. Different from the multi-phase compositing, this study suggested a promising strategy to enhance the combined mechanical and tribological performance of MAX phase coatings by M-site V solid solution for harsh applications at a high temperature of 900 °C.

1. Introduction

MAX ($M_{n+1}AX_n$, n = 1, 2, or 3) phases refer to layered high-performance ceramic materials with a close-packed hexagonal structure, where M is an early transition metal element, A is a IIIA or IVA element, and X is C or N. Because of their unique properties

* Corresponding author at: Key Laboratory of Marine Materials and Related Technologies, Zhejiang Key Laboratory of Marine Materials and Protective Technologies, Ningbo Institute of Materials Technology and Engineering, Chinese Academy of Sciences, Ningbo 315201, China.
E-mail address: kepl@nimte.ac.cn (P. Ke).

https://doi.org/10.1016/j.matdes.2022.111060
0264-1275/

similar to combining ceramics and metals [1], MAX phases have been attracting much attention in a wide range of potential applications such as nuclear stack systems and aircraft engines [2–4]. To date, more than 80 types of MAX phases have been experimentally fabricated or theoretically predicted. Among them, Cr_2AlC, the only ternary layered carbide identified in the Cr-Al-C system, displays better compatibility with superalloys [5]. Its excellent oxidation resistance and hot corrosion resistance at high temperatures are mainly due to the simultaneous presence of Al and Cr [6–10], which favor the formation of oxides as protective layers. Specifically, Cr_2O_3 formed by the oxidation of Cr has a lubricating effect at high temperatures [11], making Cr_2AlC a potential material for applications requiring high-temperature wear resistance. However, there is a scarcity in studies regarding the tribology of Cr_2AlC coatings, and a few of published works have focused on tribology at medium temperatures [12–15].

Recently, Sun et al. [16] used ab initio total energy calculations to evaluate the mechanical properties of M_2AlC, where the M element included Cr, Ti, V, Nb, and Ta. They found that of these five compositions, Cr_2AlC exhibited the highest shear, bulk, and Young's moduli. Furthermore, Cr_2AlC MAX phase coatings can be synthesized in the temperature range of 400–500 °C by physical vapor deposition (PVD) techniques, which is the lowest synthesis temperature among the MAX phase coatings currently reported [17]. Considering these features, Cr_2AlC is considered as one of the strongest protective candidates for middle/high-temperature, strain-tolerant, corrosion/wear resistant coatings used in gas turbines, nuclear claddings, and other harsh environments [18].

It should be noted that despite the physiochemical properties and facile deposition technique, one predominant challenge in utilizing the Cr_2AlC MAX phase as protective coatings under corrosion-mechanically coupled conditions is its low hardness, ranging 3.5–5.5 GPa for bulk materials and 11–15 GPa for coatings [19]. Recently, a solid solution at the M site has been attempted to enhance the mechanical performance of MAX phase coatings. For example, utilizing Zr to partially substitute Ti, Qu et al. [20] fabricated an almost pure solid solution $(Ti_{1-x}Zr_x)_3SiC_2$ MAX phase in the temperature range of 1450–1750 °C by reactive spark plasma sintering (SPS). For x = 0.17, the nano-hardness of the synthesized $(Ti_{1-x}Zr_x)_3SiC_2$ MAX phase increased to 16.3 ± 1.1 GPa, compared to that of Ti_3SiC_2 at 12.7 ± 1 GPa. Hadi et al. [21] performed density functional theory (DFT) calculations to study the effect of structural evolution on the mechanical, thermal, and electronic properties of Zr_2AlC, Nb_2AlC, and particularly the solid solution $(Zr_{1-x}Nb_x)_2AlC$ MAX phase materials. The simulation indicated that the stiffness of the solid solution $(Zr_{1-x}Nb_x)_2AlC$ increased with increasing Nb content. Since it is empirically known that the higher the Young's modulus and hardness, the lower the ability to deform plastically and absorb energy before the fracture occurs in the coatings, it is necessary to enhance both the hardness and toughness of Cr_2AlC MAX phase coatings based on their high Young's modulus (260–288 GPa) [10,22–24].

In terms of the M-site solid solution, the characteristics of the solid solution elements are assumed to play a key role in forming the MAX phase. V and Cr are adjacent atoms of the same period in the periodic table with similar atomic radii. In addition, V_2AlC and Cr_2AlC have almost the same crystal structures, which gives rise to the high solubility of V in the Cr_2AlC MAX phase and the formation of a replacement solid solution $(Cr, V)_2AlC$. A series of solid solutions $(Cr, V)_2AlC$ have been successfully prepared [25,26]. More importantly, V_2O_5 formed in a high-temperature environment as a Magnéli phase possesses good lubricity [27–29], which can greatly improve the high-temperature tribological properties of the Cr_2AlC MAX phase. (The general formula of the Magnéli phase is Me_nO_{2n-1}, Me_nO_{3n-1} or Me_nO_{3n-2}, which contain a ReO_3-type structure with atomic dislocations. So it has good lubricity [30].) In this work, we proposed a strategy using a solid solution of V at the M position to improve both the mechanical and tribological properties of the Cr_2AlC MAX phase.

In our previous work [31], Cr-Al-C coatings were successfully prepared through a facile hybrid arc/magnetron sputtering method followed by post-heat treatment. The coatings displayed a dense and mainly single-phase Cr_2AlC MAX phase with excellent oxidation resistance. Based on the solid solution strengthening concept at the M site [32], we further fabricated $(Cr, V)_2AlC$ solid solution coatings using the same hybrid technique. In particular, the effect of the V solid solution on the mechanical properties and high-temperature tribological properties of Cr_2AlC MAX phase coatings were investigated. The results indicated that the V solid solution enhanced both these properties simultaneously without deteriorating the dense structure of Cr_2AlC MAX phase coatings, as expected.

2. Experiments

2.1. Coating deposition

Cr-V-Al-C coatings with varying V content were deposited on nickel-based superalloy (GH3600, φ30 mm × 3 mm) and WC-Co carbide alloy (YG6, 10 mm × 10 mm) substrates by combined arc/-magnetron sputtering. The former was used for high-temperature friction experiments, and the latter was used for structural observation and mechanical performance testing. The detailed substrate information and schematic diagram of the deposition system have been described in our previous work [31]. Prior to the deposition, the substrates were ultrasonically cleaned with alcohol for 10 min and then placed on a vertical rotating fixture with a rotation speed of 9.5 rpm facing the targets, 5 cm apart. To improve the adhesion strength and avoid the elemental interdiffusion between the coating and substrate, a Cr interlayer (thickness of ~350 nm) was deposited by pure arc technology. The arc power of the Cr, $Cr_{75}V_{25}$ and $Cr_{50}V_{50}$ targets and the sputter power of Al target were kept at 1.0 kW and 3.0 kW, respectively. The flow rate ratio of Ar to CH_4 was 20:3, at a chamber pressure of 2.0 Pa, was introduced as a reactive gas source. The deposition process lasted for 3 h at 200 °C. In order to form the Cr_2AlC and $(Cr, V)_2AlC$ MAX phases, the as-deposited Cr-Al-C and Cr-V-Al-C coatings were subsequently annealed at 700 °C for 1.5 h in a controlled vacuum of 1.0×10^{-3} Pa. The obtained Cr_2AlC and V-substituting $(Cr, V)_2AlC$ MAX phase coatings were labeled as samples 1, 2, and 3 according to the arc targets Cr, $Cr_{75}V_{25}$, and $Cr_{50}V_{50}$, respectively.

2.2. Tribological and oxidation test

The tribological behavior of Cr_2AlC and V-substituted $(Cr, V)_2AlC$ MAX phase coatings at 900 °C in atmospheric environment was investigated using a high-temperature ball-on-disc tribometer (Anton Paar THT), which was operated in dry sliding against an Al_2O_3 ball with a diameter of 6 mm. The normal load, sliding speed, sliding distance and radius of the wear track were maintained at 2 N, 1 cm/s, 20 m and 5 mm, respectively. The heating rate and cooling rate were 9 °C/min, 3.8 °C/min, respectively. Normalized wear rates (W_R $mm^3N^{-1}m^{-1}$) were calculated using the following equation [33]:

$$W_R = \frac{d(3d^2 + 4b^2)2\pi r}{6bF_nL}$$

where d and b are the depth and width of the wear track, respectively; these were determined using a surface profilometer (Alpha-Step IQ, America). r is the radius of the wear track, F_n is the normal load, and L is the sliding distance. The wear rate of each

sample was obtained by calculating the average value of the wear rate in at least five different positions on the wear track. To reduce contingency, the high-temperature friction test of each sample was repeated two or three times, and the friction coefficient (COF) and wear rate were calculated. Since friction strongly depends on the oxidation at high temperatures, the oxides generated therein can significantly reduce the COF of the coating [29]. Therefore, oxidation characterizations such as surface and cross-sectional morphology were also conducted in this study to help analyze the friction mechanism.

2.3. Characterization techniques

The phase compositions of the coatings after preparation and friction tests were investigated using a Bruker D8 Advanced diffractometer with Cu Kα (λ = 1.5418 Å) radiation. X-ray diffraction (XRD) patterns were obtained using the Bruker TOPAS software for Rietveld refinement. The microstructure and elemental composition were analyzed using scanning electron microscopy (SEM, FEI Quanta 250 FEG) equipped with an energy dispersive X-ray spectrometer (EDS, Oxford Instruments). A confocal laser scanning microscope (Carl Zeiss, LSM 700) was used to measure the surface roughness (Sa) of the coatings. In order to observe the cross-sections of the prepared coatings and the wear track, transmission electron microscopy (TEM) and scanning TEM high-angle-annular-dark-field (STEM-HAADF) analysis were performed with a Talos F200 at an operating voltage of 200 kV. The samples were prepared using a focused ion beam (FIB; Carl Zeiss, Auriga).

The mechanical properties of the coatings, including hardness (H) and elastic modulus (E), were measured using an MTS-G200 nano-indenter in a continuous stiffness measurement mode with a Berkovich diamond tip. The indenter radius is 20 nm. The coatings were mechanically polished before testing to reduce the effect of roughness. The indentation depth was selected to be 1500 nm, and the value of hardness was chosen at a depth of 600–700 nm, which is approximately 1/10 of the coating thickness to avoid the influence of the substrates. Indentation was repeated ten times for each sample to minimize measurement error. The fracture toughness of the coatings was evaluated using a CSM scratch tester with a tapered diamond tip having a radius of 0.2 mm and cone angle of 120°. The tip was moved at a speed of 1.5 mm/min and the scratch length was 3 mm. Simultaneously, the applied load increased linearly from 0 to 90 N at a loading velocity of 44.5 N/min or maintained at 19 N. Two-dimensional (2D) and three-dimensional (3D) cross-sectional profiles of the wear tracks were comprehensively carried out using a surface profilometer (Alpha-Step IQ, USA) and a scanning white light interference microscope (3D Universal Profilometer, Rtec).

3. Results and discussion

3.1. Chemical composition and microstructure

Fig. 1 shows the phase composition and structural evolution of the coatings, as determined by XRD. As shown in Fig. 1a, the XRD patterns displayed two detectable crystalline phases for all samples, which could be attributed to Cr_2AlC and Cr, indexed by the PDF card No.00-029-0017 and No.01-088-2323, respectively. According to the enlarged view of the 2θ at 35–45° shown in Fig. 1b, both the Cr_2AlC diffraction peaks at approximately 36° and 42° shifted toward lower angles with the increase in V content in the arc targets. However, the diffraction peak at 43.5°, corresponding to the Cr phase, remained unchanged regardless of the V solid solution. These evolutions of lattice parameters suggest that the $(Cr, V)_2AlC$ solid solution structure was formed for samples 2 and 3. To quantify the changes in the lattice parameters of the coatings, Rietveld refinement was performed for the diffraction patterns, where Cr_2AlC was used as the structural model. Furthermore, the final reliability factor (R-P and R-WP) was maintained at less than 10% by repeating several refinement cycles to ensure adequate refinement accuracy. Fig. 1c–e shows the Rietveld refinement diagrams, and the calculated phase content and lattice parameters are listed in Table 1. It could be observed that the phase content of the Cr_2AlC and $(Cr, V)_2AlC$ phases in all three samples was above 90 wt%. As the V content increased, the lattice parameters *a* and *c* of the main phase increased, which further confirmed that V was successfully dissolved into the lattice of the Cr_2AlC MAX phase. Based on the EDS results in Table 2, the MAX phases in the three samples were determined to be Cr_2AlC, $(Cr_{0.76}, V_{0.24})_2AlC$, and $(Cr_{0.53}, V_{0.47})_2AlC$, corresponding to samples 1, 2, and 3, respectively.

Fig. 2 shows the surface and cross-sectional morphologies of the coatings. As illustrated in Fig. 2a–c, all three coatings exhibited dense and crack-free microstructures, although many macroparticles emerged on the coating surface. Based on our previous work [31,34], these macroparticles were mainly due to the ejection of Cr droplets during the arc evaporation of the Cr target. Moreover, with the increase in V content, the number of macroparticles on the coating surface increased, causing an increase in roughness. The surface roughness (Sa) of samples 1, 2, and 3 was (22.8 ± 3) nm, (122 ± 12) nm, (187 ± 12) nm, respectively. This could be attributed to the significant reduction in the melting point of the Cr-V alloy target compared to that of the Cr target when V partly replaced Cr to form a solid solution alloy target. Through the cross-sectional morphology, it was found that the macroparticles only appeared on the surface and did not penetrate the coating. Because these weakly boned macroparticles were prone to peel off due to the ion bombardment. However, it must be noted that the cross-sectional morphology of all three samples exhibited a dense, homogeneous structure rather than a columnar and loose crystal structure (Fig. 2d–f). Furthermore, no visible voids existed throughout the coating depth, and all coatings adhered strongly to the substrate. The coating thickness of the $(Cr, V)_2AlC$ solid solution (7.6 μm) as shown in Fig. 2e–f was similar to that of the Cr_2AlC coating (7.5 μm), indicating that the addition of V in the alloy target did not significantly affect the deposition rate.

To further evaluate the microstructure evolution of the $(Cr, V)_2AlC$ solid solution MAX phase, TEM analysis was carried out on samples 2 and 3. The detailed TEM microstructure of the Cr_2AlC could refer to our previous work [31]. As shown in Fig. 3, the coatings exhibited a dense microstructure without the presence of a columnar crystalline structure (Fig. 3a and e), confirmed by previous studies [31]. In general, the MAX phase has a hexagonal close-packed (*hcp*) crystal structure with a space group of $P6_3/mmc$, and M-layered and A-layered atoms arrange periodicity along the [000*l*] direction when the direction of electron beam is parallel to the $[11\bar{2}0]$ zones for the TEM characterization. As seen in the HRTEM images (Fig. 3b and f), the stacking sequence of the $(Cr, V)_2AlC$ MAX phase with two (Cr, V)C-slabs interleaved with a square-planar layer of Al appeared in both coatings. According to the crystal structure database, the ideal *c* lattice parameters of Cr_2AlC and V_2AlC MAX phases were 1.28 nm and 1.31 nm, respectively; it is notable that the *c* lattice parameter of the sample 2 deduced from the HRTEM (1.22 nm) was slightly lower than that of sample 3 (1.31 nm) as expected, as shown in Fig. 3c and g, originating from the increase of the content of V solid solution. According to the TEM results, as the V content increased, the trend of the *c* lattice parameter for the three samples was consistent with the above calculation results. Therefore, the TEM results further confirmed that $(Cr, V)_2AlC$ solid solution MAX phase coatings were successfully synthesized in this study.

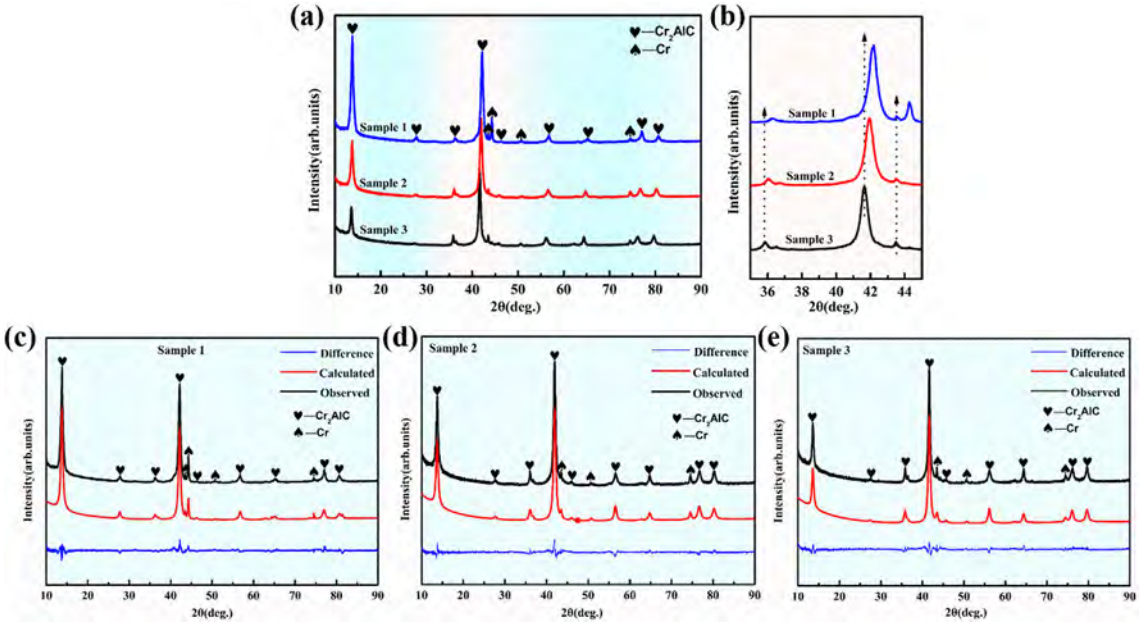

Fig. 1. XRD images of the prepared Cr-V-Al-C coatings. (a) XRD images of three samples. (b) The enlarged view of the shaded part in (a). (c), (d) and (e) Rietveld refinement diagram of samples 1, 2, and 3.

Table 1
Calculated phase content and lattice parameters of the prepared coatings.

sample	phase	phase content (wt.%)	a (Å)	c (Å)	R-P (%)	R-WP (%)
1	Cr_2AlC	90	2.87	12.88	8.34	9.6
	Cr	10	3.60			
2	$(Cr, V)_2AlC$	95	2.88	12.91	8.0	9.4
	Cr	5	3.60			
3	$(Cr, V)_2AlC$	92	2.89	12.99	6.80	9.13
	Cr	8	3.60			

Table 2
Elemental composition of the prepared coatings.

Sample	Elemental composition (at.%)				
	Cr	Al	V	C	Ni
1	48.68 ± 2.41	25.45 ± 1.96	–	25.87 ± 3.28	–
2	40.41 ± 2.76	23.14 ± 0.86	11.66 ± 0.52	24.79 ± 2.97	–
3	35.83 ± 1.55	21.06 ± 1.74	26.34 ± 1.88	16.77 ± 2.55	–

3.2. Mechanical properties

Fig. 4a shows the load-depth curves when performing nano-indentation. The curves of the three coatings were smooth and no pop-in and pop-out events were found. Bartsch et al. [35] found that when a smooth load-displacement curve is obtained, the higher the slope of the curve, the higher the energy dissipated, and the smaller the span width of the crack, which means the fracture toughness of the coating is the better. As the content of V in the coating increased, the slope of the curve increased. It is inferred that the fracture toughness of sample 3 was the best. In addition, the load on the coatings increased at the same depth (1500 nm) as the V content increased, corresponding to an increase in the hardness of the coating.

Fig. 4b shows the hardness, elastic modulus, H/E^*, and H^3/E^{*2} of the coatings. Hardness represents the resistance to plastic deformation when the indenter is depressed, and a high elastic modulus indicate great resistance to deformation under a given load [36]. The hardness and elastic modulus of the sample 1 displayed relatively low values of 16.6 ± 0.5 GPa and 261 ± 7 GPa, respectively. With increasing V content in the coating, both the hardness and elastic modulus increased steadily, mainly because of the solid solution strengthening effect [37]. Specifically, the hardness and elastic modulus of sample 3 increased by 34.3% and 23.6%, respectively, compared to those of sample 1.

The fracture toughness of the coating has a close relationship with the difficulty of forming cracks, which is a very important aspect of the mechanical properties [38,39]. Leyland et al. [40] reported that elastic strain to failure (H/E^*, where $E^* = E/(1-\nu^2)$ and ν is the Poisson's ratio) played an important role in wear control, while Johnson et al. [41] found that the ratio of plastic strain to failure (H^3/E^{*2}) indicated the ability of coatings to resist plastic deformation. Fig. 4b shows the obtained H/E^* and H^3/E^{*2} values of the coatings. As the V content in the coating increased, H/E^* and H^3/E^{*2} also increased, indicating that the fracture toughness of the solid solution coatings improved. This might originate from the solid solution $(Cr, V)_2AlC$ being uniformly strengthened by substitution. Furthermore, V has a larger radius than Cr, causing some

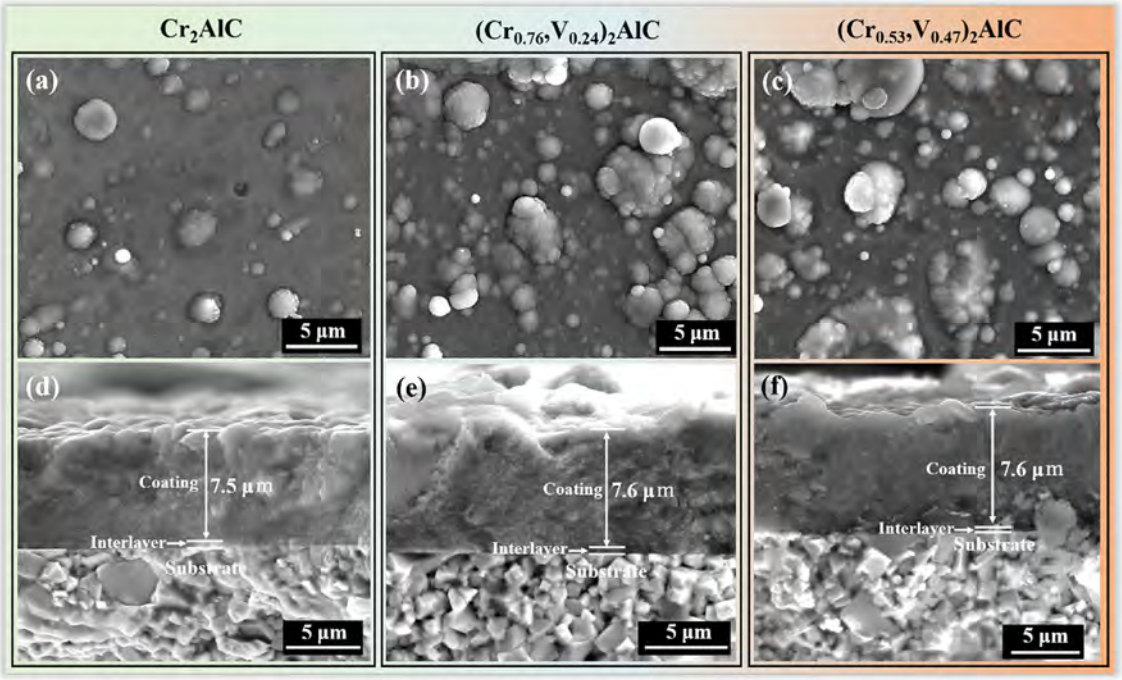

Fig. 2. Surface, cross-sectional morphology of (a) and (d) sample 1, (b) and (e) sample 2, (c) and (f) sample 3.

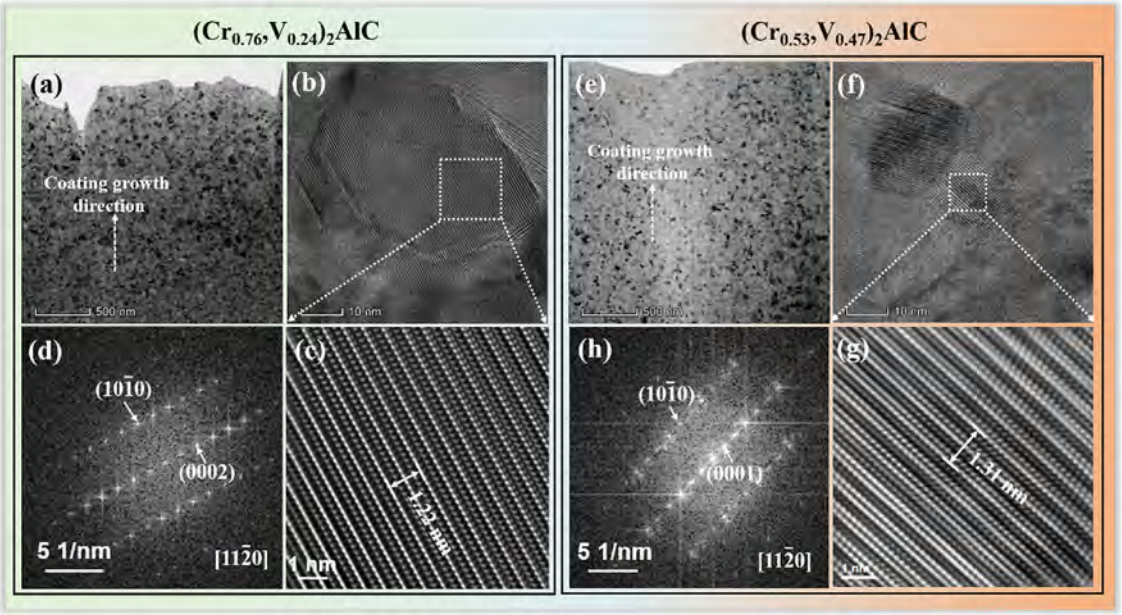

Fig. 3. TEM results of samples 2 and 3. (a) TEM bright-field image of sample 2 at low magnification. (b) HRTEM image of sample 2. (c) and (d) Enlarged image of the labeled area in (b) and the corresponding FFT results. (e) TEM bright-field image of sample 3 at low magnification. (f) HRTEM image of sample 3. (g) and (h) Enlarged image of the labeled area in (f) and the corresponding FFT results.

deformation in the original lattice. It also acted as an obstacle on the atomic scale to prevent crack spreading. Owing to the difference in the valence state between the two atoms after replacement, the row and column spacing would change to generate a stress field. When the crack tip enters the stress field, deflection under the effect of stress makes a significant contribution to toughening. For decades, it has been difficult to obtain coatings with improved toughness without sacrificing their hardness. Therefore, the crucial result is achieving the simultaneous improvement of the hardness and toughness of Cr_2AlC MAX phase coatings using a V solid solution, which provided a novel strategy to obtain hard-yet-tough MAX phase coatings.

To further understand the fracture toughness of the prepared coatings, scratch tests with progressive loads from 1 to 90 N and a constant load of 19 N were performed. Fig. 5a–c shows the corresponding scratch morphologies of samples 1, 2, and 3, respectively, under a progressive load from 1 to 90 N. As shown in Fig. 5a, the adhesion strength of sample 1 was determined to be approximately 19 N, where the first failure chip formed. When the load continued to increase, the coating peeled off severely. However,

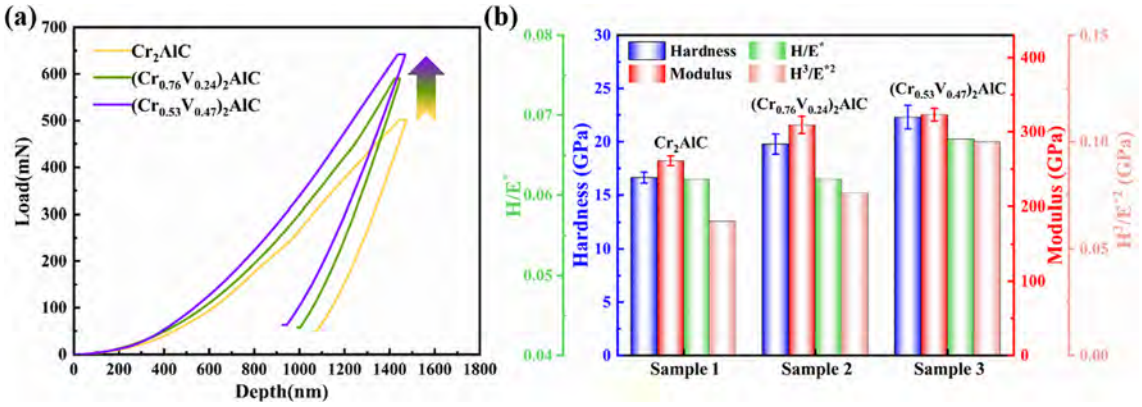

Fig. 4. (a) Load-depth curves and (b) hardness, elastic modulus, H/E^* and H^3/E^{*2} of samples 1, 2 and 3.

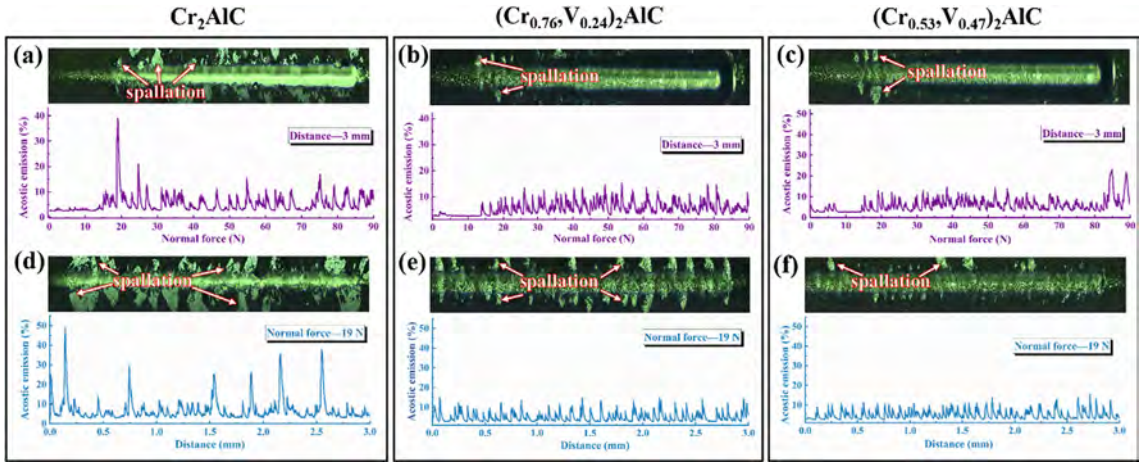

Fig. 5. The scratch morphology of samples 1, 2, and 3. (a), (b) and (c) Sample 1, 2, and 3 with progressive load from 1 to 90 N, respectively. (d), (e), and (f) Samples 1, 2, and 3 with a constant load of 19 N, respectively.

for the (Cr, V)$_2$AlC coatings with a small amount of Cr, minimal coating spalling occurred during the entire scratching process, implying that the fracture toughness of the latter was superior to that of sample 1. Fig. 5d–f illustrates the scratch morphology of samples 1, 2, and 3 under a constant load of 19 N. It is obvious that each sample underwent brittle spalling phenomenon during the entire scratching process. However, the spalling of sample 1 was the worst with many large chips, further demonstrating its poor fracture toughness. During the scratch test, the stress induced by the applied load could only be offset through large-area spalling. However, after the solid solution of the V element, the spalling morphology of the scratch scar changed from large flaking to sporadic flaking. Further, increasing the V content in the coating led to a decrease in the number of flaking debris. It can be concluded that the fracture toughness of the coating was continuously improved by the V solid solution, which agreed well with the above nanoindentation results.

3.3. Oxidation behavior at 900 °C

Fig. 6 shows the oxidized surface morphology and the corresponding EDS mapping results of samples 1–3 after the tribological tests at 900 °C. It should be noted that under the same friction temperature, samples with varying V content exhibited completely different morphologies. As shown in Fig. 6a and the inserted images, sample 1 still exhibited a metallic luster and the oxide area surface was very flat and smooth, analogous to the prepared coating in Fig. 2. Based on the EDS mapping images, Cr, V, and Al were uniformly distributed, demonstrating that the oxidation reaction of sample 1 was mild and the retained coating still exhibited the MAX phase structure of the deposited coating. However, the EDS results of area A in Table 3 demonstrate that the coating underwent a degree of oxidation.

Compared to sample 1, sample 2 underwent oxidation to dark green after the friction test at 900 °C, as shown in the inset image of Fig. 6b. Furthermore, the oxidized area exhibited a rough cauliflower-like structured surface. As the macroparticles produced by arc deposition disappeared, it could be deduced that the coating was severely oxidized. According to the corresponding EDS mapping results, the surface layer was mainly composed of Al- and Cr-forming oxides. Moreover, the elemental composition of area B in Table 3 reveals that the content of O was high, while the contents of V and C were relatively low.

Interestingly, after the tribological tests, the surface of sample 3 appeared to have an ice-flower-like texture, as shown in Fig. 6c. Consequently, it was speculated that a low melting point phase melted during the test and recrystallized during the cool-down period. Because of the presence of liquid lubrication, the wear track was too shallow to provide an accurate wear rate within the measurement errors. The elemental distribution in the EDS mapping images corresponding to the oxidized region was not uniform. Nevertheless, the V-rich areas were poor in Cr and Al, with C disappearing, as marked by the orange ellipse in Fig. 6c. The remaining O and V elements were the main components in the C area (Table 3),

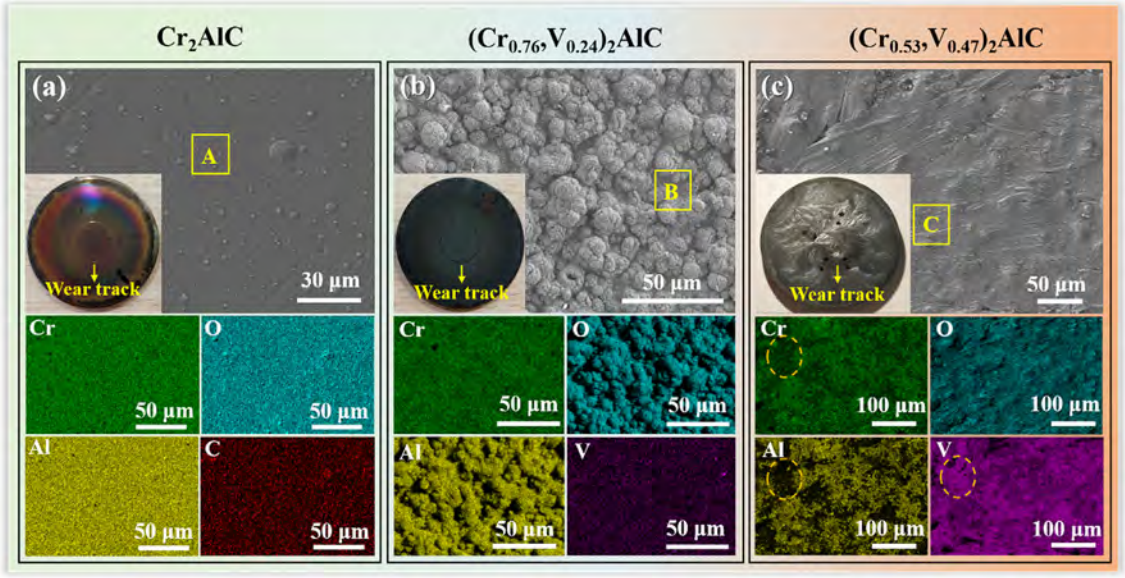

Fig. 6. Oxidized surfaces and the corresponding EDS mapping images at 900 °C (a) sample 1; (b) sample 2; (c) sample 3.

Table 3
Elemental composition at different positions of oxidation area (corresponding to the letter number in Fig. 6).

Sample ID	Elemental composition (at.%)					
	Cr	Al	O	V	C	Ni
A	32.30	20.41	35.02	–	12.27	–
B	19.04	22.71	50.61	1.51	4.98	–
C	4.19	6.91	64.52	24.37	–	–

demonstrating the completely oxidized state of the coating. Vice versa, the Cr- and Al- rich areas had little V. In this case, it could be said that the liquid lubrication in the friction experiment was attributed to the presence of the V-O phase.

Fig. 7 presents the cross-sectional morphology and the corresponding EDS line scans of samples 1–3 after the tribological tests at 900 °C. As seen in Fig. 7a, sample 1 exhibited a uniform thickness of 7 μm, which was slightly lower than that of the prepared coating. From the corresponding EDS line scan, a very thin oxide layer with a thickness of 0.28 μm was identified, which is more clearly illustrated in the enlarged image of the yellow rectangle in the inset of Fig. 7a. In addition, there was a diffusion zone with a thickness of 1.80 μm without interfacial damage or cracking. This suggests that a close fusion was successfully realized after cooling to room temperature, which confirmed that the Cr_2AlC MAX phase is a promising candidate as a high-temperature, corrosion-resistant, and strain-tolerant diffusion barrier for Ni-based superalloys [5]. Generally, during the thermal process, diffusion of coating elements into the substrate occurs possibly causing a decrease in the thickness and properties compared with the features of the prepared coating.

With the increase in V content, however, the interface between the $(Cr, V)_2AlC$ MAX phase coating and the substrate was evident and no diffusion zone was visible, as shown in Fig. 7b and c. The

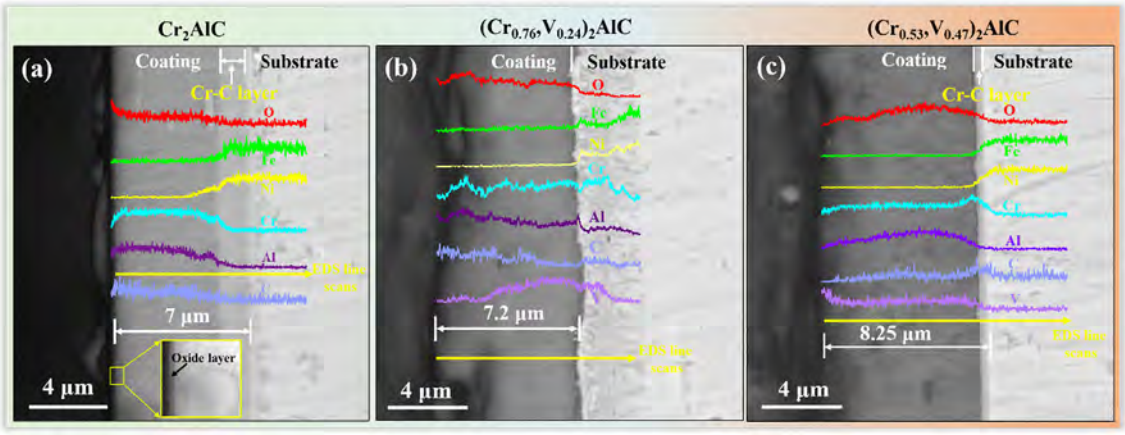

Fig. 7. Cross-sectional morphology of the oxidized area and the corresponding EDS line scans along the marked yellow line of (a) sample 1, (b) sample 2, and (c) sample 3.

coating was oxidized throughout, and the original structure was completely destroyed. Furthermore, the oxide scale was uneven, the thickness measured at the position shown in Fig. 7b and Fig. 7c was 7.2 μm and 8.25 μm, respectively. Note that no C element existed in sample 3, corresponding to a greater degree of oxidation and increase in thickness. In addition, a Cr-C layer with a thickness of 0.36 μm was observed between the oxidized coating and the substrate (Fig. 7c).

3.4. Tribological performances at 900 °C

Fig. 8a shows the sliding friction curves of samples 1–3 after the friction tests at 900 °C. All three samples exhibited relatively stable friction curves without large fluctuations during the entire tribology test, indicating that the formation of oxide phases during friction sufficiently contributed to lubrication. At the same temperature, the average COF decreased with an increase in the V content in the coating, which was approximately 0.36, 0.35, and 0.27, respectively, as shown in Fig. 8b. The addition of V reduced the oxidation resistance of the Cr_2AlC coating, that is, higher the V content, more oxidation occurred and more oxide phases were generated to benefit lubrication. In particular, a large amount of liquid lubrication emerged for sample 3 in such a high-temperature environment, significantly reducing the COF. The wear rate of sample 2, $(6.18 \pm 0.59) \times 10^{-4}$ $mm^3N^{-1}m^{-1}$, was nearly ten times that of sample 1, $(7.88 \pm 0.89) \times 10^{-5}$ $mm^3N^{-1}m^{-1}$. According to the previous oxidation results, sample 2 underwent severe oxidation at 900 °C. Its original structure was significantly destroyed, leading to poor wear resistance and high wear rate. In the case of sample 3, the wear rate could not be obtained because the wear track during the friction test was too shallow to be accurately calculated (Fig. 6c). However, it was safe to assume that the wear rate of sample 3 was the lowest among the three samples, indicating that the tribological performance of sample 3 at 900 °C was the best.

To gain insight into the tribological behavior after the friction test, Fig. 9 presents the 3D and 2D profiles of the three samples using a white light interference scanning microscope and a surface profilometer, respectively. The wear tracks of the three samples exhibited different appearances. Sample 1 showed a narrow and shallow wear track (Fig. 9a) with a width and depth of 69 μm and 2.58 μm, respectively, corresponding to a low wear rate. However, the wear track of sample 2 was relatively rough with a width of 410 μm and a depth of 4.93 μm, which was nearly six times and two times that of sample 1, respectively. As a consequence, sample 2 exhibited a higher wear rate than sample 1 (Fig. 9b). It should be noted that there were two protrusions in the wear track in sample 2, determined by 3D topography, which were speculated to be the adhesion and accumulation of oxide scale during the friction. Further increasing the V content in the coating, very large fluctuations similar to the roughness result emerged in the 2D morphology of sample 3. Simultaneously, a very shallow and inconspicuous wear track was observed in the 3D topography. In addition, the rough surface was occupied by many particles of different sizes, which was probably caused by the uneven solidification of the molten V-O phase during the cooling process. It is worth noting that the depths of the wear tracks of the three samples were all less than the thickness of the deposited coatings, suggesting that no coating was worn after friction at 900 °C in this study.

To address the wear mechanism, the wear tracks of the coatings and the corresponding elemental distribution mapping images were further examined by SEM, as shown in Fig. 10. The EDS elemental compositions of the different areas (labeled in the SEM micrograph) are summarized in Table 4. In particular, the evolution of the worn surface is comprehensively discussed. After friction at 900 °C, the wear track of sample 1 shown in Fig. 10a was very smooth and flat, with no signs of abrasive wear, adhesive wear, or accumulated wear debris. This is in line with the results shown in Fig. 9a. Moreover, both the elemental distribution and the oxidation state of the wear track were evenly distributed in the coating, despite the slightly enriched oxygen appearing on the left side of the wear track. Together with the good oxidation resistance of sample 1, the smooth surface with the minimal roughness of the deposited coating favored good lubrication against the Al_2O_3 ball, as expected. These results further demonstrate the potential of the Cr_2AlC coating as a protective layer in a high-temperature friction environment.

With an increase in the V content of the coating, sample 2 exhibited a clear and smooth wear track similar to that of sample 1, as shown in Fig. 10b. No obvious abrasive or accumulated wear debris along the wear track was observed. However, the enlarged surface of the rectangular yellow area (Fig. 10c) presented many long rod-shaped abrasive grains, which were referred to in the enriched areas of V and Ni (circled by the red ellipses). This was contrary to the exposed wear track without abrasive grains composed of Cr- and Al-enriched oxides on the coating surface (circled by white ellipses). Considering that sample 2 experienced serious oxidation at 900 °C and possible consumption of generated oxide phases, the Ni element appearing on the wear track surface might be attributed to the elemental out-diffusion of the substrate at the chosen temperature. Further increasing the V solid solution content in the Cr_2AlC coating led to a distinct friction morphology that was different from those in samples 1 and 2, as shown in Fig. 10d–e. In addition, both the wear track and oxidation zone noted by

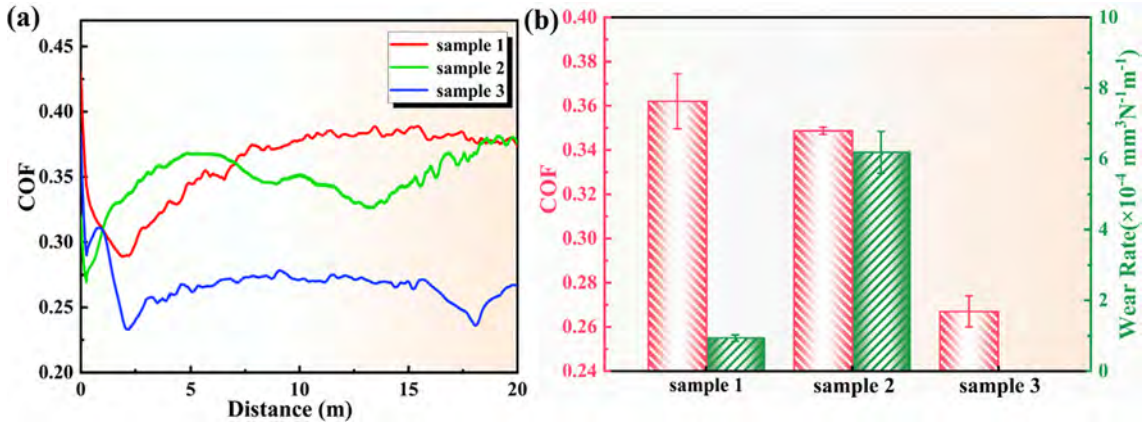

Fig. 8. (a) Friction curve, (b) COF and wear rate for samples 1, 2, and 3 after ball-on-disk friction test performed at 900 °C.

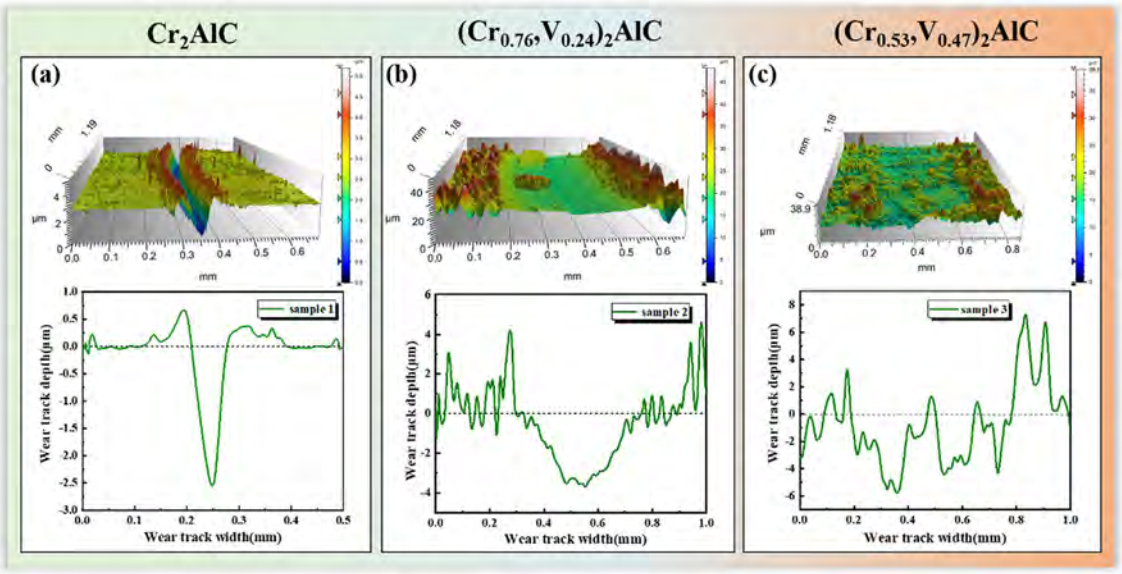

Fig. 9. 3D cross-sectional profiles of the wear tracks at 900 °C and the corresponding 2D wear track depth profiles were attached below of (a) sample 1, (b) sample 2, and (c) sample 3.

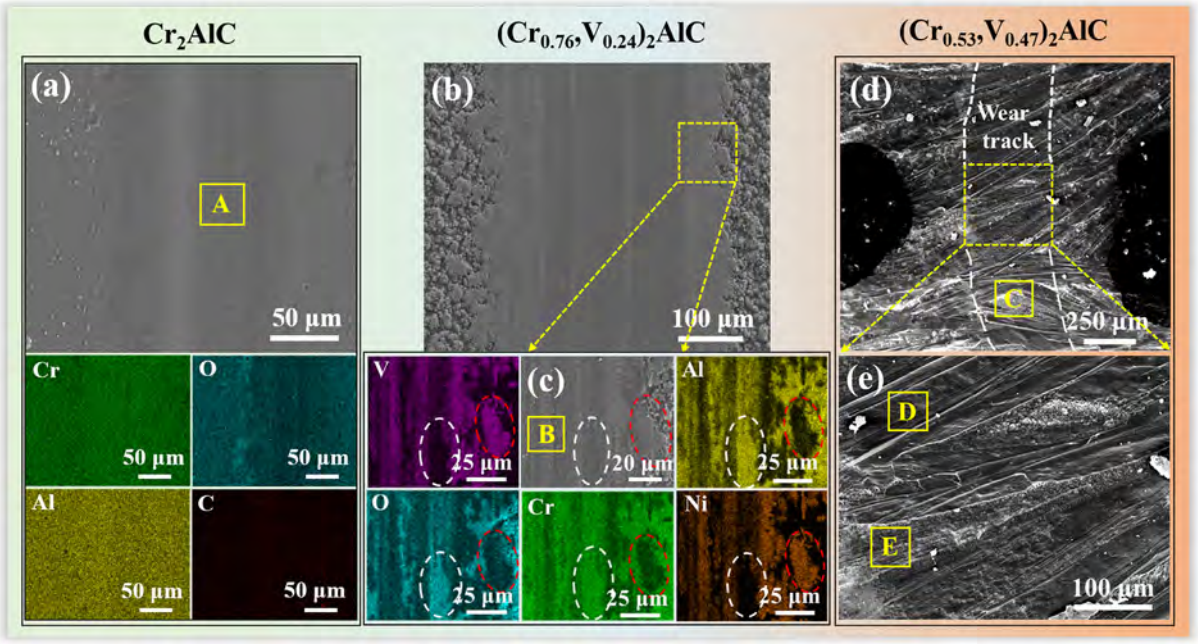

Fig. 10. SEM micrograph of wear tracks and the corresponding EDS elemental mapping images: (a) sample 1, (b) sample 2, (c) enlarged view of the yellow rectangle in b, (d) sample 3, (e) enlarged view of the yellow rectangle in d.

Table 4
Elemental composition at different positions of wear tracks (corresponding to the letter number in Fig. 10).

Sample ID	Elemental composition (at.%)					
	Cr	Al	O	V	C	Ni
A	36.06	19.64	29.76	–	14.54	–
B	12.98	9.84	39.58	12.57	10.16	14.88
C	6.48	7.49	65.08	18.12	2.83	–
D	3.69	3.43	57.55	34.32	1.01	–
E	4.75	4.73	55.79	31.91	2.82	–

areas C, D, and E displayed an ice-flower-like morphology composed of the dominant V and O elements because of the re-solidification of the V-O phase. This result also provides evidence of liquid lubrication from the V-O phase during the high-temperature friction process.

To accurately describe the phase composition of the coating after friction at 900 °C, Fig. 11 shows the phase composition of the wear track and oxidized surface of the coatings by XRD measurement. For sample 1, the XRD pattern depicts the peaks of Cr_2AlC and Cr_7C_3 without other oxide peaks, implying that the oxide layer was too thin to be detected or the formed oxides exhibited an amorphous nature, as illustrated in Fig. 7a and Fig. 10a. In this aspect, even though sample 1 underwent a slight oxidation, it retained most of its composition with the pristine coating. For sample 2, however, the strong diffraction peaks of Al_2O_3 and Cr_2O_3 without information about the prepared coating were observed as a consequence of the severe oxidization and the highest wear rate. In addition, the diffraction peaks of Ni_3V and $Ni(VO_3)_2$ also appeared, because the Ni diffusing from the substrate might react with V, as deduced from Fig. 10c. By further increasing the V content, a large number of diffraction peaks of V_2O_5 for sample 3 appeared. At the same time, a small amount of diffraction peaks of Cr_2O_3 and Al_2O_3 were also observed. During the friction at 900 °C, the melted V_2O_5 phases provided sufficient liquid lubrication, thereby reducing the wear and consumption of the coating, which finally caused the smallest COF and wear rate among the three samples. The design concept was verified to improve the high-temperature tribology of Cr_2AlC MAX phase coatings by substituting part of Cr with V.

4. Discussion

To achieve a better understanding of the tribological mechanism, Fig. 12 shows cross-sectional views of the wear tracks by TEM and STEM after dry sliding tests at 900 °C. For sample 1, the coating still exhibited a very dense structure, and no extra pores or grain boundaries were observed. Moreover, the upper wear track was a combined double oxide layer composed of the top Cr-O layer and the bottom Al-O layer, followed by a Cr-C layer containing some Al-O grains distributed evenly. The STEM image based on the different atomic masses also shows a clear distinction between Cr and Al elements. Because a uniform and dense oxide layer was formed on the coating surface, the internal diffusion of oxygen was prevented, and the coating could not be further oxidized. At the same time, the flat oxide layer also suppressed the appearance of abrasive and adhesive wear, which favored the coating with a very low COF and wear rate at 900 °C, resulting in good tribological properties for sample 1.

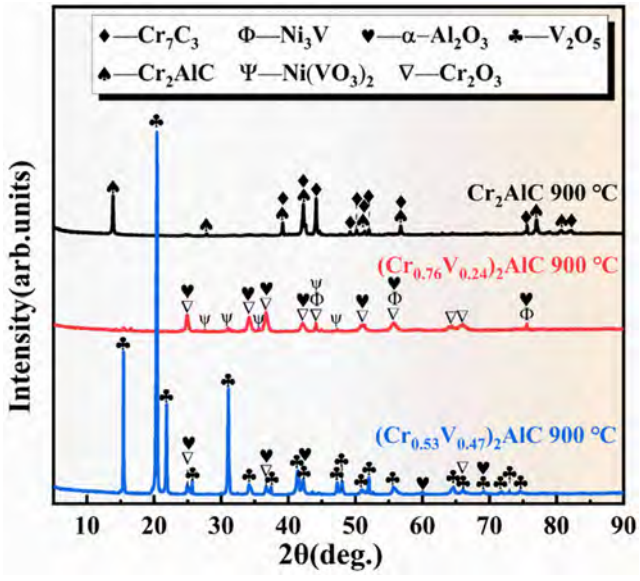

Fig. 11. XRD patterns of samples 1, 2, and 3 after friction test at 900 °C.

With the increase in the V solid solution, as in sample 2, the coating was entirely oxidized, and no delamination of the coating was observed, as shown in Fig. 12b. Moreover, there were many grains with different sizes and obvious grain boundaries, as shown in Fig. 12c. Although Cr and Al had the same crystal grains as that of sample 1, the difference is that the grain boundaries were filled mainly by the V oxides. Owing to the limited V content, many pores were formed between the grain boundaries, leading to the loose structure shown in Fig. 12d. At the same time, the slight diffusion of Ni from the substrate into the coating further deteriorated the structure of the coating. As a result, sample 2 exhibited poor wear resistance during friction at 900 °C.

In the case of sample 3, which had a higher V content, four obvious crystal grains were observed in the cross-sectional morphology of the wear track (Fig. 12e). According to the mapping images, these crystal grains were mainly identified as oxides of Cr and Al, and the rest were composed of glassy-like V_2O_5 and a small amount of amorphous carbon. In addition, because the amount of V_2O_5 was large enough to fill all the grain boundaries, a very dense whole structure was obtained without pores, which was different from that of sample 2. Once again, it was confirmed that, with higher V content in the Cr_2AlC coating, both the molten V_2O_5 and the dense structure contributed to the excellent liquid lubrication during the friction process at 900 °C.

Elaborating the structural evolution of the three samples during the friction test at 900 °C, Fig. 13 illustrates the schematic diagram of the wear mechanism. First, in our study, both the COF and wear rate of the Cr_2AlC MAX phase coating with a small amount of Cr at 900 °C were relatively low, demonstrating that the coatings were very promising protective coating candidates for high-temperature harsh friction environments. For the Cr_2AlC MAX phase coating with high purity, dense double-layer oxides, including Cr_2O_3 and Al_2O_3, were formed on the wear track surface during 900 °C friction. In particular, the outermost Cr_2O_3 layer aided lubrication at high temperatures, resulting in a lower COF [11]. The dense Al_2O_3 layer offered further protection for the coating by preventing the internal diffusion of oxygen. Alternatively, the surface roughness of the coating was quite low, due to the suppressed large macroparticles generated by arc deposition, which also prevented the occurrence of abrasive wear and had a smooth wear track surface morphology just like "glaze". It should be noted that even a diffusion zone was also generated at the interface between the coating and substrate, owing to the high diffusion activity of Ni and Fe in the substrate at such high temperatures, there were no cracks in the diffusion zone. This indicates the gradient transition from substrate to coating, which resulted in a strong combination and good adhesion between the coating and substrate after cooling 900 °C to room temperature.

However, adding a small amount of V to the Cr_2AlC coating significantly reduced the high-temperature oxidation resistance (sample 2). While V was solid-dissolved to the M position of the MAX phase, V replaced Cr to bond with Al and C. Nevertheless, V was extremely easy to be oxidized, and once V was oxidized at 900 °C, the M-A and M-X bonds would be destroyed. In this case, the Al and C atoms with non-bonding electrons would prefer to combine with oxygen. At the same time, once this process started, the internal diffusion of oxygen was stimulated and caused more serious oxidation for the entire coating at 900 °C. Thereafter, the formed grains with a large range of crystal sizes generated many

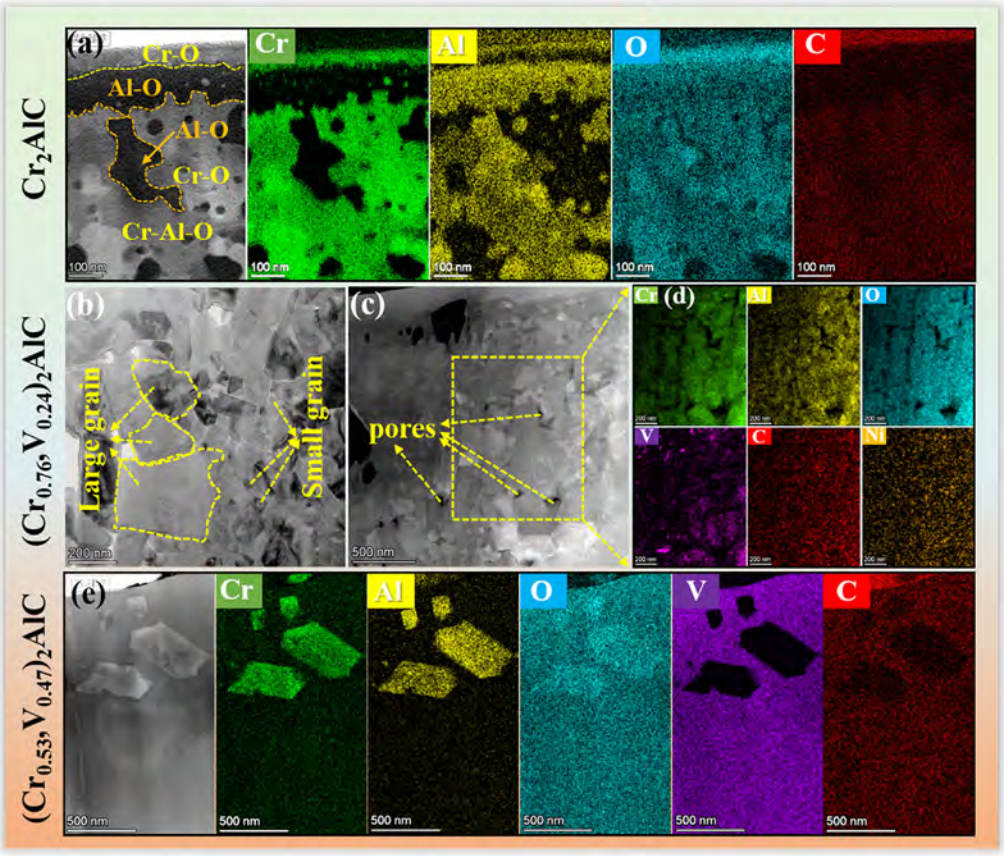

Fig. 12. Cross-sectional images of the wear tracks: (a) STEM image and the corresponding EDS elemental mapping images of sample 1, (b) and (c) TEM and STEM image of sample 2, respectively, (d) corresponding EDS elemental mapping images of the yellow rectangle in c, (e) STEM image and the corresponding EDS elemental mapping images of sample 3.

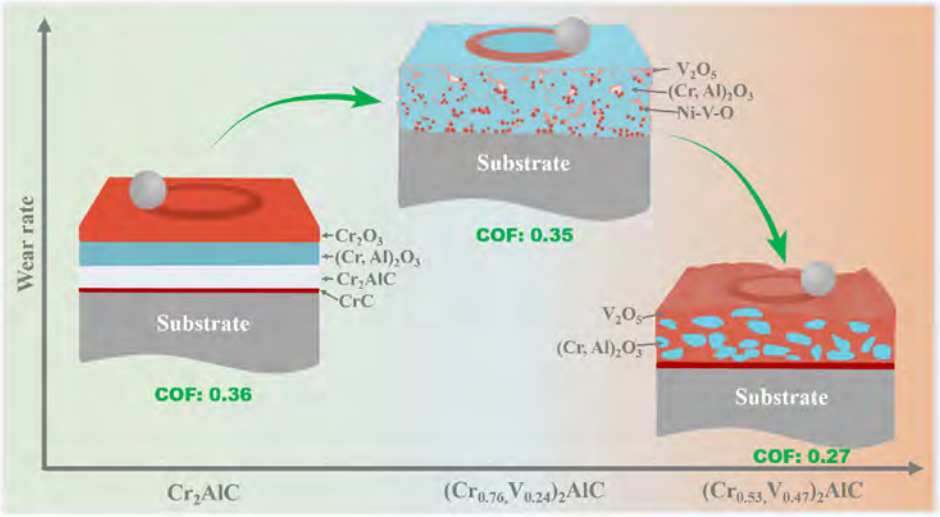

Fig. 13. Schematic diagram of the friction mechanism of sample 1, sample 2, and sample 3 at 900 °C.

pores at the grain boundaries. Because there was no dense oxide layer on the coating surface to provide protection, the maximum wear rate was obtained for this coating with a loose structure. It was raised that, according to the deep wear track, the out-diffusion of Ni element from substrate was also observed and the Ni atoms reacted with V to form Ni_3V and $Ni(VO_3)_2$. Consequently, the coating obtained by sacrificing a certain degree of wear resistance could not provide sufficient lubrication to significantly reduce the COF, where sample 2 displayed the worst tribological properties among the three samples at 900 °C.

When the V content in the coating was higher (sample 3), a large amount of melted V_2O_5 phases were formed during the friction process, favoring a wide range of liquid lubrication. Specifically, the Al_2O_3 and Cr_2O_3 crystal grains were surrounded by a

large amount of molten V_2O_5, generating a dense structure combining soft and hard phases. During friction, the wear track was constantly filled owing to the liquid fluidity. Together with the support of the hard crystal grains, collapse of the coating was prevented and it exhibited the lowest COF, in which the wear track was too shallow to accurately calculate the wear rate. After the coating was greatly oxidized, a sufficient amount of molten V_2O_5 appeared as a blocking barrier to the external penetration of oxygen. This promoted the combination of unoxidized Cr and C atoms inside the coating and the formation of the Cr-C layer between the coating and the substrate with non-uniform thickness, as expected. It should be noted that even when the generated V_2O_5 at high temperatures has a good lubricating effect, it is easily consumed with sliding time. Therefore, it is empirically known that V-based coatings mostly display a high wear rate at high temperatures; in particular, a medium temperature of approximately 700 °C is preferred for superior tribological behaviour [42]. In this regard, the most important result is that the excellent wear resistance with both low COF and wear rate at 900 °C is reported for Cr_2AlC MAX phase coatings by solid dissolving V in the coating, which also provides a promising strategy to extend the wide application of V-based coatings for harsh high-temperature environments.

5. Conclusion

In this study, we successfully prepared Cr_2AlC, V-substituted $(Cr_{0.76}, V_{0.24})_2AlC$, and $(Cr_{0.53}, V_{0.47})_2AlC$ MAX phase coatings with a small amount of Cr using a hybrid arc/magnetron sputtering method together with post-heat treatment. The effects of the V solid solution on the mechanical properties and high-temperature tribological behavior of Cr_2AlC MAX phase coatings were investigated. The results showed that all the Cr_2AlC and $(Cr, V)_2AlC$ MAX phase coatings demonstrated a dense structure with no obvious defects, despite the presence of V, increasing the roughness of the Cr_2AlC coatings. Compared to the Cr_2AlC coating, the hardness and elastic modulus of $(Cr_{0.53},V_{0.47})_2AlC$ were improved by 34.3% and 23.6%, respectively. Evidently, the V solid solution also significantly enhanced the toughness of the Cr_2AlC MAX phase coating owing to the refined lattice distortion. During the friction at 900 °C, the Cr_2AlC coating presented an average COF of 0.36, and a relatively low wear rate of 7.88×10^{-5} $mm^3N^{-1}m^{-1}$, because of the formation of a bilayer oxide comprising a Cr_2O_3 layer on top and an Al_2O_3 layer on the bottom. Owing to the liquid lubricating effect of the molten V_2O_5 phases, the COF was reduced significantly with increasing V content in the Cr_2AlC coating. In contrast to the $(Cr_{0.76}, V_{0.24})_2AlC$ coating with a loose structure and adhesive wear, it is worth noting that the $(Cr_{0.53}, V_{0.47})_2AlC$ coating resulted in an excellent low COF and wear rate, originating from the formation of a dense structure of Cr_2O_3 and Al_2O_3 hard grains wrapped by soft molten V_2O_5. These results not only indicate that optimizing the solid solution fraction of V in Cr_2AlC coating can favor the achievement of hard-yet-tough as well as high-temperature tribological properties in MAX phase coatings, but also bring forward a great potential to extend the wide applications of V-based self-lubricated coatings at harsh high temperatures (900 °C).

CRediT authorship contribution statement

Zhenyu Wang: Conceptualization, Investigation, Data curation, Project administration, Writing – original draft, Funding acquisition. **Cuicui Wang:** Validation, Methodology, Writing – review & editing. **Yupeng Zhang:** Resources, Visualization, Data curation. **Aiying Wang:** Writing – review & editing, Supervision, Funding acquisition. **Peiling Ke:** Project administration, Writing – review & editing, Supervision, Funding acquisition.

Declaration of Competing Interest

The authors declare that they have no known competing financial interests or personal relationships that could have appeared to influence the work reported in this paper.

Acknowledgement

This research was supported by the National Natural Science Foundation of China (51901238, 52171090, 52025014, 51875555), and CAS Interdisciplinary Innovation Team (292020000008).

References

[1] M.W. Barsoum, The $M_{N+1}AX_N$ phases: A new class of solids: thermodynamically stable nanolaminates, Prog. Solid State Chem. 28 (1-4) (2000) 201–281, https://doi.org/10.1016/S0079-6786(00)00006-6.
[2] Z.Y. Wang, J. Sun, B.B. Xu, Y.R. Liu, L. Wang, P.L. Ke, A.Y. Wang, Reducing the self-healing temperature of Ti_2AlC MAX phase coating by substituting Al with Sn, J. Eur. Ceram. Soc. 40 (2020) 197–201, https://doi.org/10.1016/j.jeurceramsoc.2019.09.009.
[3] Y.C. Zhou, X.H. Wang, Deformation of polycrystalline Ti_2AlC under compression, Mater. Res. Innovat. 5 (2) (2001) 87–93, https://doi.org/10.1007/s100190100132.
[4] W. Tian, ZhengMing Sun, H. Hashimoto, Y. Du, Compressive deformation behavior of ternary compound Cr_2AlC, J. Mater. Sci. 44 (1) (2009) 102–107, https://doi.org/10.1007/s10853-008-3113-0.
[5] M. Sokol, J. Yang, H. Keshavan, M.W. Barsoum, Bonding and oxidation protection of Ti_2AlC and Cr_2AlC for a Ni-based superalloy, J. Eur. Ceram. Soc. 39 (4) (2019) 878–882, https://doi.org/10.1016/j.jeurceramsoc.2018.10.019.
[6] D.B. Lee, S.W. Park, Oxidation of Cr_2AlC between 900 and 1200 °C in air, Oxid. Met. 68 (2007) 211–222, https://doi.org/10.1007/s11085-007-9071-0.
[7] S. Li, L. Xiao, G. Song, X. Wu, W.G. Sloof, S. van der Zwaag, Y. Zhou, Oxidation and crack healing behavior of a fine-grained Cr_2AlC ceramic, J. Am. Ceram. Soc. 96 (3) (2013) 892–899, https://doi.org/10.1111/jace.12170.
[8] D.E. Hajas, M. to Baben, B. Hallstedt, R. Iskandar, J. Mayer, J.M. Schneider, Oxidation of Cr_2AlC coatings in the temperature range of 1230 to 1410 °C, Surf. Coat. Technol. 206 (4) (2011) 591–598, https://doi.org/10.1016/j.surfcoat.2011.03.086.
[9] M. Ougier, A. Michau, F. Lomello, F. Schuster, H. Maskrot, M.L. Schlegel, High-temperature oxidation behavior of HiPIMS as-deposited Cr-Al-C and annealed Cr_2AlC coatings on Zr-based alloy, J. Nucl. Mater. 528 (2020) 151855, https://doi.org/10.1016/j.jnucmat.2019.151855.
[10] Z.J. Lin, M.S. Li, J.Y. Wang, Y.C. Zhou, High-temperature oxidation and hot corrosion of Cr_2AlC, Acta Mater. 55 (18) (2007) 6182–6191, https://doi.org/10.1016/j.actamat.2007.07.024.
[11] J.H. Ouyang, S. Sasaki, Effects of different additives on microstructure and high-temperature tribological properties of plasma-sprayed Cr_2O_3 ceramic coatings, Wear 249 (1-2) (2001) 56–66, https://doi.org/10.1016/S0043-1648(01)00530-0.
[12] S. Gupta, D. Filimonov, V. Zaitsev, T. Palanisamy, M.W. Barsoum, Ambient and 550 ℃ tribological behavior of select MAX phases against Ni-based superalloys, Wear 264 (2008) 270–278, https://doi.org/10.1016/j.wear.2007.03.011.
[13] S. Gupta, D. Filimonov, T. Palanisamy, T. El-Raghy, M.W. Barsoum, Ta_2AlC and Cr_2AlC Ag-based composites-New solid lubricant materials for use over a wide temperature range against Ni-based superalloys and alumina, Wear 262 (11-12) (2007) 1479–1489, https://doi.org/10.1016/j.wear.2007.01.028.
[14] E.I. Zamulaeva, E.A. Levashov, E.A. Skryleva, T.A. Sviridova, P.V. Kiryukhantsev-Korneev, Conditions for formation of MAX phase Cr_2AlC in electrospark coatings deposited onto titanium alloy, Surf. Coat. Technol. 298 (2016) 15–23, https://doi.org/10.1016/j.surfcoat.2016.04.058.
[15] S. Gupta, D. Filimonov, T. Palanisamy, M.W. Barsoum, Tribological behavior of select MAX phases against Al_2O_3 at elevated temperatures, Wear 265 (3-4) (2008) 560–565, https://doi.org/10.1016/j.wear.2007.11.018.
[16] Z. Sun, S.a. Li, R. Ahuja, J.M. Schneider, Calculated elastic properties of M_2AlC (M=Ti, V, Cr, Nb and Ta), Solid State Chem. 129 (9) (2004) 589–592, https://doi.org/10.1016/j.ssc.2003.12.008.
[17] J.J. Li, L.F. Hu, F.Z. Li, M.S. Li, Y.C. Zhou, Variation of microstructure and composition of the Cr_2AlC coating prepared by sputtering at 370 and 500 °C, Surf. Coat. Technol. 204 (23) (2010) 3838–3845, https://doi.org/10.1016/j.surfcoat.2010.04.067.
[18] J. Gonzalez-Julian, G. Mauer, D. Sebold, D.E. Mack, R. Vassen, Cr_2AlC MAX phase as bond coat for thermal barrier coatings: Processing, testing under thermal gradient loading, and future challenges, J. Am. Ceram. Soc. 103 (4) (2020) 2362–2375, https://doi.org/10.1111/jace.16935.
[19] J. Gonzalez-Julian, J. Llorente, M. Bram, M. Belmonte, O. Guillon, Novel Cr_2AlC MAX-phase/SiC fiber composites: Synthesis, processing and tribological response, J. Eur. Ceram. Soc. 37 (2) (2017) 467–475, https://doi.org/10.1016/j.jeurceramsoc.2016.09.029.

[20] L.S. Qu, G.P. Bei, B. Stelzer, H. Rueß, J.M. Schneider, D.X. Cao, S. van der Zwaag, W.G. Sloof, Synthesis, crystal structure, microstructure and mechanical properties of $(Ti_{1-x}Zr_x)_3SiC_2$ MAX phase solid solutions, Ceram. Int. 45 (2019) 1400–1408, https://doi.org/10.1016/j.ceramint.2018.10.030.
[21] M.A. Hadi, U. Monira, A. Chroneos, S.H. Naqib, A.K.M.A. Islam, N. Kelaidis, R.V. Vovk, Phase stability and physical properties of $(Zr_{1-x}Nb_x)_2AlC$ MAX phases, J. Phys. Chem. Solids 132 (2019) 38–47, https://doi.org/10.1016/j.jpcs.2019.04.010.
[22] Z. Lin, M. Zhuo, Y. Zhou, M. Li, J. Wang, Atomic scale characterization of layered ternary Cr_2AlC ceramic, J. Appl. Phys. 99 (7) (2006) 076109, https://doi.org/10.1063/1.2188074.
[23] W.-B. Tian, P.-L. Wang, G.-J. Zhang, Y.-M. Kan, Y.-X. Li, Mechanical Properties of Cr_2AlC Ceramics, J. Am. Ceram. Soc. 90 (5) (2007) 1663–1666, https://doi.org/10.1111/j.1551-2916.2007.01634.x.
[24] M. Imtyazuddin, A.H. Mir, M.A. Tunes, V.M. Vishnyakov, Radiation resistance and mechanical properties of magnetron-sputtered Cr_2AlC thin films, J. Nucl. Mater. 526 (2019) 151742, https://doi.org/10.1016/j.jnucmat.2019.151742.
[25] W.B. Tian, Z.M. Sun, H. Hashimoto, Y.L. Du, Synthesis, microstructure and properties of $(Cr_{1-x}V_x)_2AlC$ solid solutions, J. Alloy. Compd. 484 (1–2) (2009) 130–133, https://doi.org/10.1016/j.jallcom.2009.04.111.
[26] Z.M. Sun, T. Sonoda, H. Hashimoto, A. Matsumoto, Synthesis of MAX phase (Cr, V)$_2$AlC thin films, Sci. Technol. Adv. Mat. 750 (2013) 1–6, https://doi.org/10.4028/www.scientific.net/MSF.750.1.
[27] N. Fateh, G.A. Fontalvo, C. Mitterer, Tribological Properties of Reactive Magnetron Sputtered V_2O_5 and VN-V_2O_5 Coatings, Tribol. Lett. 30 (1) (2008) 21–26, https://doi.org/10.1007/s11249-008-9307-4.
[28] N. Fateh, G.A. Fontalvo, G. Gassner, C. Mitterer, Influence of high-temperature oxide formation on the tribological behaviour of TiN and VN coatings, Wear 262 (9-10) (2007) 1152–1158, https://doi.org/10.1016/j.wear.2006.11.006.
[29] K. Kutschej, P.H. Mayrhofer, M. Kathrein, P. Polcik, C. Mitterer, Influence of oxide phase formation on the tribological behaviour of Ti-Al-V-N coatings, Surf. Coat. Technol. 200 (5-6) (2005) 1731–1737, https://doi.org/10.1016/j.surfcoat.2005.08.044.
[30] A. Magnéli, Structures of the ReO_3-type with Recurrent Dislocations of Atoms: 'Homologous Series' of Molybdenum and Tungsten Oxides, Acta Crystallogr. 6 (6) (1953) 495–500, https://doi.org/10.1107/S0365110X53001381.
[31] Z.Y. Wang, G.S. Ma, L.L. Liu, L. Wang, P.L. Ke, Q.J. Xue, A.Y. Wang, High-performance Cr_2AlC MAX phase coatings: Oxidation mechanisms in the 900–1200 °C temperature range, Corros. Sci. 167 (2020) 108492, https://doi.org/10.1016/j.corsci.2020.108492.
[32] M.A. Ali, M.M. Hossain, M.A. Hossain, M.T. Nasir, M.M. Uddi, M.Z. Hasan, A.K.M. A. Islam, S.H. Naqib, Recently synthesized $(Zr_{1-x}Ti_x)_2AlC$ ($0 \leq x \leq 1$) solid solutions: Theoretical study of the effects of M mixing on physical properties, J. Alloy. Compd. 743 (2018) 146–154, https://doi.org/10.1016/j.jallcom.2018.01.396.
[33] C.C. Chang, H.W. Chen, J.W. Lee, J.G. Duh, Development of Si-modified CrAlSiN nanocomposite coating for anti-wear application in extreme environment, Surf. Coat. Technol. 284 (2015) 273–280, https://doi.org/10.1016/j.surfcoat.2015.06.090.
[34] Z.Y. Wang, J.Z. Liu, L. Wang, X.W. Li, P.L. Ke, A.Y. Wang, Dense and high-stability Ti_2AlN MAX phase coatings prepared by the combined cathodic arc/sputter technique, Appl. Surf. Sci. 396 (2017) 1435–1442, https://doi.org/10.1016/j.apsusc.2016.11.183.
[35] M. Bartsch, I. Mircea, J. Suffner, B. Baufeld, Interfacial Fracture Toughness Measurement of Thick Ceramic Coatings by Indentation, Key Eng. Mater. 290 (2005) 183–190, https://doi.org/10.4028/www.scientific.net/KEM.290.183.
[36] G.S. Kim, S.Y. Lee, J.H. Hahn, S.Y. Lee, Synthesis of CrN/AlN superlattice coatings using closed-field unbalanced magnetron sputtering process, Surf. Coat. Technol. 171 (1-3) (2003) 91–95, https://doi.org/10.1016/S0257-8972(03)00244-5.
[37] J. Zhu, H. Jiang, F. Wang, Q.i. Ma, Synthesis, microstructure evolution, and mechanical properties of $(Cr_{1-x}V_x)_2AlC$ ceramics by in situ hot-pressing method, J. Mater. Res. 29 (10) (2014) 1168–1174, https://doi.org/10.1557/jmr.2014.91.
[38] J. Musil, Z. Čiperová, R. Čerstvý, Š. Kos, Hard alloy films with enhanced resistance to cracking, Vacuum 188 (2021) 110186, https://doi.org/10.1016/j.vacuum.2021.110186.
[39] V.A. Lapitskaya, T.A. Kuznetsova, S.A. Chizhik, A.I. Komarov, Y.I. Frolov, A.S. Romanyuk, Study of the Crack Resistance of Microarc Oxidation Coatings after Laser Doping with Zirconium Oxide, Tech. Phys+ 64 (11) (2019) 1609–1614, https://doi.org/10.1134/S1063784219110173.
[40] A. Leyland, A. Matthews, On the significance of the H/E ratio in wear control: a nanocomposite coating approach to optimised tribological behaviour, Wear 246 (1-2) (2000) 1–11, https://doi.org/10.1016/S0043-1648(00)00488-9.
[41] K.L. Johnson, Contact Mechanics, Cambridge University Press, Cambridge, 1985.
[42] C.C. Wang, B.B. Xu, Z.Y. Wang, H. Li, L. Wang, R.D. Chen, A.Y. Wang, P.L. Ke, Tribological mechanism of (Cr, V)N coating in the temperature range of 500–900 ℃, Tribol. Int. 159 (2021) 106952, https://doi.org/10.1016/j.triboint.2021.106952.